Journal of Hazardous Materials 439 (2022) 129504

Contents lists available at ScienceDirect

Journal of Hazardous Materials

journal homepage: www.elsevier.com/locate/jhazmat

Research Paper

Novel Ni foam catalysts for sustainable nitrate to ammonia electroreduction

Anna Iarchuk [a,b], Abhijit Dutta [a,*], Peter Broekmann [a,b,**]

[a] Department of Chemistry, Biochemistry and Pharmaceutical Science, University of Bern, Freiestrasse 3, 3012 Bern, Switzerland
[b] National Centre of Competence in Research (NCCR) Catalysis, University of Bern, Freiestrasse 3, 3012 Bern, Switzerland

HIGHLIGHTS

- Novel Ni foam catalyst is synthesized by means of a dynamic hydrogen bubble template assisted electrodeposition process.
- The 3D foam morphology of the catalyst is demonstrated to crucially govern its overall catalytic performance.
- Ni foam is exhibited outstanding selectivity toward nitrate electroreduction.
- More than 95% of the FE of NH_3 production was achieved within the low potential range from − 0.1 to − 0.3 V *vs.* RHE.
- Trapping NO_3^- RR intermediates inside the primary macroporosity contributed to the excellent catalytic performance.

GRAPHICAL ABSTRACT

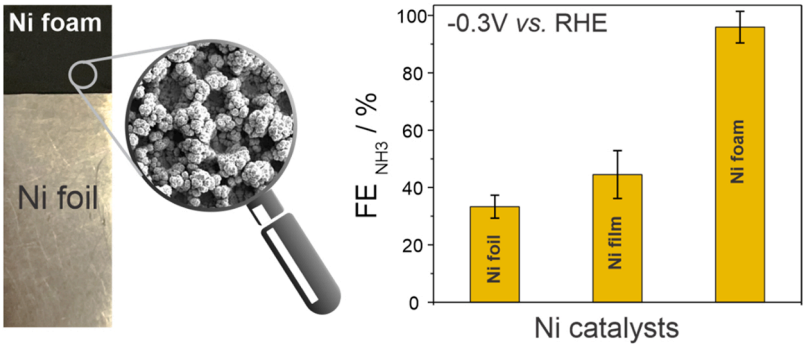

ARTICLE INFO

Editor: Danmeng Shuai

Keywords:
Porous material
Ni foam
Waste water treatment
Electrochemical Nitrate Reduction
Ammonia synthesis

ABSTRACT

Electrochemical nitrate reduction (NO_3^-RR) is considered a promising approach to remove environmentally harmful nitrate from wastewater while simultaneously producing ammonia, a product with high value. An important consideration is the choice of catalyst, which is required not only to accelerate NO_3^-RR but also to direct the product selectivity of the electrolysis toward ammonia production. To this end, we demonstrate the fabrication of novel Ni foam catalysts produced through a dynamic hydrogen bubble template assisted electrodeposition process. The resulting foam morphology of the catalyst is demonstrated to crucially govern its overall electrocatalytic performance. More than 95% Faradaic efficiency of ammonia production was achieved in the low potential range from –0.1 to –0.3 V *vs.* RHE. Hydrogen was found to be the only by-product of the nitrate reduction. Intriguingly, no other nitrogen containing products (*e.g.*, NO, N_2O, or N_2) formed during electrolysis, thus indicating a 100% selective (nitrate→ammonia) conversion. Therefore, this novel Ni foam catalyst is a highly promising candidate for truly selective (nitrate→ammonia) electroreduction and a promising alternative to mature copper-based NO_3^-RR benchmark catalysts. Excellent catalytic performance of the novel Ni foam catalyst was also observed in screening experiments under conditions mimicking those in wastewater treatment.

* Corresponding author.
** Corresponding author at: Department of Chemistry, Biochemistry and Pharmaceutical Science, University of Bern, Freiestrasse 3, 3012 Bern, Switzerland
E-mail addresses: abhijit.dutta@unibe.ch (A. Dutta), peter.broekmann@unibe.ch (P. Broekmann).

https://doi.org/10.1016/j.jhazmat.2022.129504
Received 2 March 2022; Received in revised form 20 June 2022; Accepted 28 June 2022
Available online 1 July 2022

1. Introduction

In the past several decades, numerous anthropogenic activities (*e.g.*, intensive farming) have led to substantial perturbations in the nitrogen cycle (Canfield et al., 2010; Galloway et al., 2003; Gruber and Galloway, 2008; Yang and Gruber, 2016). In particular, nitrate pollution in soil and groundwater has become a serious environmental threat with high potential to affect human health and consequently destabilize entire ecosystems worldwide (Galloway et al., 2008). The continually increasing production and use of nitrogen-based fertilizers (Yang and Gruber, 2016; *e.g.*, ammonium nitrate and ammonium sulfate), other industrial activities (*e.g.*, generation of low-level nuclear wastewater (Katsounaros et al., 2009; van Langevelde et al., 2021), and the production of pharmaceuticals (Chauhan and Srivastava, 2020)) together generate billions of tons of nitrate-containing wastewater annually (Jones et al., 2021). This unfortunate development has resulted in a steady increase in nitrate (NO_3^-) concentrations in surface waters and groundwaters, and alarmingly elevated nitrate concentrations as high as 1500 mg L^{-1} have been observed in heavily polluted areas (Jacks and Sharma, 1983). According to the recommendations of the World Health Organization, the maximum nitrate concentration in drinking water should be limited to below 50 mg L^{-1} (Chauhan and Srivastava, 2020; Su et al., 2016). High concentrations of nitrate (and nitrite) in drinking water can lead to methemoglobinemia in infants and gastrointestinal cancer in adults (Su et al., 2016).

A major anthropogenic contributor to nitrogen cycle perturbation is the Haber-Bosch process (Gruber and Galloway, 2008; Yang and Gruber, 2016), which is used to produce more than 150 million tons of ammonia annually (Ghavam et al., 2021). Ammonia is among the most important platform chemicals in the chemical industry and is an essential raw material for the production of fertilizers at large industrial scales (Ghavam et al., 2021). Ammonia synthesis requires the high-temperature and high-pressure reaction of nitrogen and hydrogen, which not only consumes enormous amounts of energy but also substantially adds to anthropogenic CO_2 emissions, because the required hydrogen is typically derived from environmentally harmful steam reforming processes (Ghavam et al., 2021; Wang et al., 2018). Therefore, electrochemical conversion of nitrate has excellent potential to contribute to both (i) the removal of environmentally harmful nitrates from various forms of wastewater (Chauhan and Srivastava, 2020; Katsounaros et al., 2009; van Langevelde et al., 2021; Lu et al., 2021) and (ii) the sustainable production of "green" ammonia (Bunea et al., 2022; van Langevelde et al., 2021; Lu et al., 2021). In this respect, electrochemical nitrate reduction (NO_3^-RR) to ammonia clearly provides greater potential environmental and industrial benefits than the mature methods of non-electrochemical wastewater treatment, whose aim is only to separate nitrate from wastewater. These mature methods are often based on ion exchange (Samatya et al., 2006), reverse osmosis (Epsztein et al., 2015), or electrodialysis (Dong Xu et al., 2018). In addition, electrolysis approaches have been used to remove nitrate from wastewater, but again only with the aim to transform nitrate into dinitrogen—a process often referred to as denitrification (Duca and Koper, 2012; van Langevelde et al., 2021).

In the future, NO_3^-RR to ammonia might become not only economically feasible but also truly sustainable, particularly if surplus renewable energy from solar radiation, wind power, and hydroelectric sources is used as an energy input for the endergonic nitrate reduction. Among other electrocatalytic processes (*e.g.*, CO_2RR (Jhong et al., 2013; Qiao et al., 2014; Whipple and Kenis, 2010) and N_2RR (Martín et al., 2019; S. Wang et al., 2018; L. Wang et al., 2018)), NO_3^-RR to ammonia is considered a key element of the "power-to-X" approach. Of note, ammonia not only is a valuable intermediate in the chemical industry but also, owing to its high energy density of 4.3kWh kg^{-1}, is a highly promising carbon-free energy carrier expected to play a key role in the "energy transition" from fossil fuels to renewable energy (L. Wang et al., 2018; S. Wang et al., 2018; Wang et al., 2020). Several experimental factors govern the product selectivity of electrocatalyzed reactions and are commonly expressed in terms of the Faradaic efficiency (FE) or the corresponding partial current density (PCD) for the production of the desired product. Among various factors, the choice of catalyst/electrode material most strongly influences the resultant product distribution and the achievable partial and total current densities (TCDs). Precious metals, such as Pt (Kato et al., 2017; Taguchi and Feliu, 2007; Yang et al., 2014), Rh (Yang et al., 2014), and Ru (Li et al., 2020), have been reported to be active toward NO_3^-RR but partially favor products other than ammonia (*e.g.*, NO_2^- and N_2). In addition, their NO_3^-RR performance is often limited by the parasitic hydrogen evolution reaction (*HER*), which occurs on these catalyst materials at high rates at particularly low applied overpotentials, thus interfering with the targeted NO_3^-RR (Taguchi and Feliu, 2007). In addition, high material costs in combination with material scarcity will impede the use of these precious metals in future NO_3^-RR applications. Therefore, research efforts are currently directed toward the development of more abundant, lower-cost NO_3^-RR electrocatalysts. Cu based materials exhibit excellent performance toward NO_3^-RR, yielding ammonia as the main electrolysis product (Abdallah et al., 2014; Wang et al., 2020). However, previous studies have also demonstrated that pure Cu catalysts often undergo oxidative dissolution or irreversible surface poisoning, both of which lead to undesired catalyst degradation (Dima et al., 2003). Moreover, NO_3^-RR over Cu catalysts often show undesirable formation of NO_2^- as a parasitic by-product (Abdallah et al., 2014; Reyter et al., 2006).

Further improvements in known catalyst materials and the search for new catalyst concepts therefore must address NO_3^-RR product selectivity, particularly the catalyst's structural and chemical stability during extended electrolysis. For example, Wang et al. have reported that co-alloying of Cu with 50% Ni significantly improves the performance of NO_3^-RR, which can be performed at particularly low applied overpotentials (FE_{NH3} = 99%; PCD_{NH3} = 90 mA cm^{-2} achieved in 1 M KOH + 100 mM KNO_3, pH 14, E = –0.1 V *vs.* the reversible hydrogen electrode (RHE)) (Wang et al., 2020). Beyond improving the energy efficiency, this binary CuNi alloy has demonstrated higher stability than that of pure Cu catalysts (Wang et al., 2020). However, a further increase in Ni content up to 70% causes a substantial loss in NO_3^-RR selectivity, thus resulting in a relatively low FE_{NH3} of 38% (1 M KOH + 1 mM KNO_3, pH 14, E = –0.06 V *vs.* RHE) (Wang et al., 2020). In apparent accordance with this reported trend, pure nanoparticulate Ni catalysts have been found to exhibit an even lower FE_{NH3} value of only 11% (1 M KOH + 1 mM KNO_3, pH 14, E = –0.06 V *vs.* RHE) (Wang et al., 2020). The electrocatalytic performance of commercial Ni foams has been studied by Zheng et al. (Zheng et al., 2021), who have reported a FE_{NH3} of 53.3%. NH_3 selectivity can be further increased through self-activation of the Ni electrodes, which has been reported to originate from *in situ* formation of an $Ni(OH)_2$ film on the Ni support (denoted $Ni(OH)_2$ @Ni) (Zheng et al., 2021). Several studies have emphasized the major role of catalyst morphology in the resultant NO_3^-RR efficiency (Abdallah et al., 2014; Wang et al., 2020; Wang et al., 2020). In this context, Zhang et al. (2018) have compared commercially available Ni foams (sponges) with CuNi composite materials derived from Cu deposition onto an Ni foam support. The electrodeposited porous Cu layer introduces additional active sites to the catalyst, thus increasing the nitrate removal efficiency from 10% to 99.2%. However, the CuNi composite catalyst has been found to remain non-selective regarding the final NO_3^-RR product (NH_3, N_2, *etc.*) (Zhang et al., 2018).

Reports describing high NO_3^-RR performance of pure Ni [Zhang et al. (2021)] or Ni-rich electrocatalysts are rare. The present work demonstrates that highly porous Ni foams electrodeposited onto a Ni foil support exhibit superior electrocatalytic characteristics, achieving more than 95% FE_{NH3} in the low potential range from –0.1 to –0.3 V *vs.* RHE. The dynamic hydrogen bubble template (DHBT) electrodeposition approach, using a high geometric current density of –3 A cm^{-2}, is

demonstrated herein to be an easily performed, fast method for the fabrication of Ni foams within 10–60 s without a need for further catalyst activation, *e.g.*, in the form of thermal annealing or anodization. We demonstrate that these pure Ni foam catalysts show superior performance toward NO_3^-RR in terms of product selectivity and catalyst durability, thus making them a viable alternative to mature copper-based NO_3^-RR catalysts.

2. Experimental methods

The Ni foams used as NO_3^-RR catalysts were fabricated through the DHBT (Shin et al., 2004; Shin and Liu, 2004) assisted electrodeposition process, with as-received Ni foils (Fig. S1) serving as the support electrode (0.25 mm thick, Alfa Aesar, 99.5% metal basis). The geometric surface area exposed to the electrolyte was 1 cm^2. This surface area was obtained by masking the Ni foil supports with PTFE tape before electrodeposition (Fig. S2). The aqueous plating bath (pH ~4.5) contained 1.5 M NH_4Cl (Sigma-Aldrich, ≥ 99.5%) as the supporting electrolyte, 0.12 M $NiSO_4$ (Sigma-Aldrich, ≥ 98%) as the Ni source, and 0.2 mg L^{-1} polyalkylene glycol (poly(ethylenglycol)-block-poly(propyleneglycol)--block-poly(ethylenglycol), Sigma-Aldrich, M_w = 8400 g mol^{-1}) as a plating additive. The galvanostatic electrodeposition process was conducted with a three-electrode setup (Fig. S3a) wherein the masked Ni foil served as the working electrode (WE), a Pt foil served as the counter electrode (CE), and an $Ag/AgCl_{3\ M}$ electrode (Metrohm, double junction design) served as the reference electrode (RE). A geometric current density of j_{geo} = –3 A cm^{-2} was applied for 5, 10, 20, 30, 40, 50, and 60 s, thus yielding Ni foams with varying thickness and pore size distribution (Table S1). After emersion from the plating bath, the formed Ni foams were thoroughly rinsed with Milli-Q water (18.2 MΩ cm and TOC value below 5 ppb, Millipore) and kept under Milli-Q water for ~1 h to completely remove residual traces of electrolyte (particularly NH_4^+ ions). Ni foams were deposited on both sides of the Ni foil support (Fig. S4).

For reference measurements, Ni film catalysts were prepared from electrodeposited Ni foams (removal of the pore structure). For this purpose, electrodeposited Ni foams (20 s deposition time) were transferred into a small vial containing isopropanol and sonicated in an ultrasonic bath sonicator. Ni powders were then obtained by evaporating the isopropanol solvent at 40 °C for 12 h. For the ink formulation, the dried Ni powders were mixed with isopropanol and 5 w% Nafion, then sonicated for 30 min. The prepared ink was painted onto a carbon support (type A8, Fuel Cell, USA). The catalyst loading was ~3 mg cm^{-2}.

X-ray powder diffractograms were recorded with a Bruker D8 diffractometer with CuK_α radiation (λ = 0.1540, I = 40 mA) generated at 40 keV acceleration voltage. Diffractograms were measured in the 2θ range from 10° to 90°, with a scan rate of 1° min^{-1}. The obtained diffractogram patterns were compared with the Joint Committee on Powder Diffraction standards for Ni and NiO (Ni-JCPDS: 04–0850, NiO-JCPDS: 73–1523).

The surface morphology of the as-received Ni foils was characterized with atomic force microscopy (Nanosurf FlexAFM V2 system, Tap150Al-G silicon cantilevers) before electrodeposition (Fig. S1). The structural analysis of the Ni foam morphologies was conducted before and after electrolysis through scanning electron microscopy (SEM) with a Zeiss Gemini 450 instrument equipped with an InLens secondary electron and a backscattered electron detector. For the InLens and backscattered electron detection modes, accelerating voltages (electron currents) of 3.0 kV (100 pA) and 20 kV (1.5 nA) were used as standard settings. AZtec 4.2 software (Oxford Instruments) was applied to acquire energy dispersive X-ray (EDX) point spectra and the respective 2D elemental mappings.

All further electrochemical experiments were performed with an H-type electrolysis cell in a three-electrode configuration (Fig. S3b), in which electrodeposited Ni foam served as the WE, a Pt foil served as the CE, and $Ag/AgCl_{3\ M}$ (Pine research, 3.5 mm outer diameter and 74 mm length) was used as the RE. To estimate the electrochemically active surface area (ECSA) of the electrodeposited Ni foam catalysts, we applied two voltammetric approaches based on (i) double-layer capacitance and (ii) (Faradaic) peak current measurements. For the capacitance method, cyclic voltammograms were recorded in 0.1 M KOH (Sigma-Aldrich, reagent grade) solution in the potential range from 0.025 to 0.175 V *vs.* RHE (Fig. S5a). The applied potential sweep rate was 10 mV s^{-1}. The current difference at 0.088 V *vs.* RHE was used for the ECSA estimation (Fig. S5b). For the (Faradaic) peak current method, potential sweep-rate dependent CVs were recorded in an electrolyte solution containing 1 mM dimethyl viologen dichloride ($DMVCl_2$; Sigma-Aldrich, 98%) and 0.1 M K_2SO_4 (Sigma-Aldrich, ≥ 99.0%) in a range from 10 to 500 mV s^{-1} (Fig. S6a–f). The reversible reduction of the dimethyl viologen di-cation (DMV^{2+}) to its corresponding radical mono-cation ($DMV^{\bullet+}$) according to

$$DMV^{2+} + e^- \rightleftharpoons DMV^{\bullet+} \quad \text{(R1)}$$

was used to probe the ECSA of the Ni foams. ECSA values were estimated on the basis of the Randles-Ševčík equation

$$j_p = 2.69 \times 10^5 \times n^{2/3} \times A \times c \times D^{1/2} \times \nu^{1/2} \quad (1)$$

where j_p refers to the (Faradaic) peak current density (normalized to the geometric surface area of 1 cm^2), n is the number of electrons transferred in the reaction, A (cm^2) is the ECSA, D (cm^2 s^{-1}) is the diffusion coefficient of the redox-active species ($D = 5.5 \cdot 10^{-6}$ cm^2 s^{-1}), and ν (V s^{-1}) is the potential sweep rate. The ECSA values were derived from the linear regression of j_p *vs.* $\nu^{1/2}$ (Fig. S6 g–I, Table S1). Of note, the Randles-Ševčík equation was originally derived for planar disk macroelectrodes rather than the porous materials studied herein. However, several studies have successfully applied this approach to porous electrode materials yielding linear j_p *vs.* $\nu^{1/2}$ relationships in the scan-rate dependent CV measurements, thus confirming the applicability of this method even in cases with non-planar porous electrodes (Dutta et al., 2020a, 2020b, 2016, 2017, 2021b).

NO_3^-RR experiments were performed with an H-type electrolysis cell in a three-electrode configuration (Fig. S3b), wherein electrodeposited Ni foam served as the WE, a Pt foil served as the CE, and $Ag/AgCl_{3\ M}$ (Pine research) served as the RE. The catholyte and anolyte compartments were separated by an anion exchange membrane (Sustainion X37–50 RT) and filled for standard catalyst screening experiments with 1 M KOH electrolyte solution (pH ~14) containing 0.1 M KNO_3 (Sigma-Aldrich, ≥99.0%). Before electrolysis, the catholyte was purged for 30 min with Ar gas (99.999%, Carbagas, Switzerland) to remove dissolved oxygen and prevent the oxygen reduction reaction, which is considered a parasitic side-reaction to NO_3^-RR. In the catalyst screening experiments, nitrate electrolyses were performed potentiostatically in a range from −0.7 V to –1.6 *vs.* $Ag/AgCl_{3\ M}$. All electrode potentials reported herein were *iR*-corrected (cell resistance determined with the current interrupt method in Nova software (Autolab)). For comparability, all potentials were further converted to the RHE scale according to:

$$E_{RHE}(V) = E_{Ag/AgCl(3M)}(V) + 0.210\ V + 0.0591\ V \cdot pH \quad (2)$$

Aliquots of the catholyte were collected after 30 min of electrolysis and subjected to quantitative ammonia (NO_3^-RR product) and nitrate (NO_3^-RR reactant) analysis, unless otherwise stated. Ammonia quantification was performed through the standard indophenol blue method (Fig. S7a). For this purpose, 20 µL of the catholyte aliquots was diluted with 1.98 mL Milli-Q water and mixed with 1 mL 0.05 M $NaClO_4$ (Sigma-Aldrich, reagent grade); 2 mL of 1 M NaOH (Sigma-Aldrich, >98.0%) containing 5 wt% salicylic acid (Sigma Aldrich, ≥99.0%) and 5 wt% sodium citrate (Sigma Aldrich, ≥99.0%); and 200 µL of 1 wt%

sodium nitroferricyanide (Sigma Aldrich, ≥99%). After a reaction time of ~1 h, UV–vis absorption spectra were recorded from 450 to 900 nm with a PerkinElmer Lambda 900 UV–vis/NIR spectrometer. The characteristic absorption maximum of the indophenol derivative was observed at a wavelength of λ = 658 nm. The indophenol (ammonia) quantification was based on calibration curves derived from a dilution series using standard ammonium ion solution (Sigma Aldrich, analytical standard). Representative calibration measurements are presented in Fig. S7b,c,d.

The FE_{NH3} was determined as the ratio of the charge consumed for the NH_3 production and the total charge (Q_{tot}) passed through the cell during electrolysis F according to

$$FE_{NH3} = \frac{n \times F \times c_{NH3} \times V}{Q_{tot}} \times 100\% \quad (3)$$

The total charge Q_{tot} (C) passed through the cell during the electrolysis was derived from integration of the respective electrolysis current *vs.* electrolysis time traces. F refers to the Faraday constant (96485 C mol^{-1}), c_{NH_3} (mol L^{-1}) denotes the spectroscopically determined NH_3 concentration, V (L) represents the volume of the catholyte ($V = 0.007L$), and n is the number of transferred electrons. The nitrate to ammonia conversion is a coupled electron-proton reduction involving the transfer of eight electrons according to

$$NO_3^- + 9H^+ + 8e^- \rightarrow NH_3 + 3H_2O \quad (R2)$$

or

$$NO_3^- + 6H_2O + 8e^- \rightarrow NH_3 + 9OH^- \quad (R3)$$

depending on the solution pH.

To exclude NO_3^-RR products other than NH_3, we probed the concentration of NO_3^- in the catholyte, as compared with the detected ammonia concentration, over time. Quantification of NO_3^- and NO_2^- (the latter of which is a possible side-product of the NO_3^-RR) was based on ion-exchange chromatography measurements performed with a Metrohm 940 Professional IC Vario instrument operated with MagIC Net 3.3 software. Catholyte solutions were diluted 100-fold before the IC analysis.

Hydrogen was found to be the only by-product of the NO_3^-RR over the Ni electrocatalysts. In a selected case study (Supplementary materials) we quantified hydrogen during NO_3^-RR through online gas-chromatography. For this purpose, Ar gas was passed through the catholyte at a flow rate of 30 mL min^{-1}. The headspace of the electrolysis cell was connected to a gas sampling loop of a gas chromatograph (GC 8610 C, SRI Instruments). A GC run was conducted every 600 s during the 30 min electrolysis. Argon (99.9999%, Carbagas) was used as the carrier gas. The GC was equipped with a packed Hayesep D column 3 m in length. A thermal conductivity detector was used to quantify the H_2 gas concentration. The GC was calibrated with a known concentration of hydrogen before quantification. The partial current of the hydrogen formed during electrolysis (I_{H_2}) was calculated according to

$$I_{H2} = \frac{c_{H2} \times \nu \times F \times z}{10^6 \times V_m} \quad (4)$$

where c_{H_2} (ppm) refers to the hydrogen concentration, ν (L s^{-1}) is the gas flow rate, F represents the Faraday constant (C mol^{-1}), and V_m (L mol^{-1}) indicates the molar gas volume at 1 atm pressure and room temperature. The FE of hydrogen production (FE_{H2}) was calculated by dividing the respective partial current by the total current

$$FE_{H2} = \frac{I_{H2}}{I_{total}} \times 100\% \quad (5)$$

3. Results and discussion

3.1. Preparation and characterization of Ni foam catalysts

An important aspect of NO_3^-RR catalyst design is the creation of high-surface area materials. Most successful catalyst concepts in the field have relied on the use of nanoparticulate (colloidal) catalysts.(Li et al., 2020; Wang et al., 2020) A clear advantage of this classical approach is that the entire spectrum of mature colloid chemistry can be applied to synthesize nano-objects with various shapes, morphologies, and size distributions. Herein, we introduce an alternative concept of NO_3^-RR catalyst fabrication based on an additive- and template-assisted metal electrodeposition route (Shin et al., 2004; Shin and Liu, 2004; Vesztergom et al., 2021), which was demonstrated to be highly versatile and complementary to the common colloid approach of catalyst design. Metal foams offer a large surface area that not only is accessible to reactants but also enables fast, multi-dimensional electron transport pathways (Vesztergom et al., 2021; Zhu et al., 2017). For the creation of highly porous foam-type materials, we used hydrogen gas bubbles as a geometric template that temporarily forms during the electrodeposition process of the primary metal (*e.g.*, Ni) on both the planar support electrode and the emerging porous catalyst film. The origin of the vigorous hydrogen gas bubble formation is the reductive decomposition of the acidic aqueous plating bath. In this metal foaming process, fairly harsh deposition conditions were applied in the form of high (geometric) current densities (*e.g.*, –3 A cm^{-2}) (Vesztergom et al., 2021). The source for the HER under these extreme conditions is not only the reduction of protons (reaction R4)

$$2H^+ + 2e^- \rightarrow H_2 \quad (R4)$$

but also the reductive splitting of water (reaction R5)

$$2H_2O + 2e^- \rightarrow H_2 + 2OH^- \quad (R5)$$

The basic concept of the so-called dynamic hydrogen bubble template (DHBT) deposition process is depicted in Fig. 1a. H_2 bubbles are generated by reactions R4 and R5, thus disrupting the growth of the Ni layer and consequently acting as a dynamic template. Micropores in the submicron range and macropores in the 10–100 μm size range are formed in the deposit, as a result of the growth of metal around small or larger coalesced bubbles generated on the surface (Vesztergom et al., 2021). With the DHBT method, extreme cathodic overpotentials are used, so that the rates of the primary metal deposition and the secondary HER become comparable, thereby determining the obtained 3D foam architecture (Vesztergom et al., 2021). However, other factors beyond the reaction rates may determine the resulting surface morphology of the deposited metal foam, such as the nucleation, growth, and detachment of the surface generated bubbles; related convective effects caused by bubble formation; local alkalinization of the near-electrode solution layers (R4 and R5) and its consequences on the chemistry of metal deposition; and the action of additives (Vesztergom et al., 2021). Of note, in the present case, both the ammonium cations and the PEG-PPG-PEG polymers act as plating additives (surfactants) influencing hydrogen bubble formation/detachment and the Ni foam growth characteristics on various length scales. Fig. 1b depicts an optical micrograph and an SEM micrograph of a representative Ni foam deposited on a planar Ni foil. In contrast to the support electrode, the electrodeposited Ni foams typically show a black appearance (denoted Ni black, Fig. S2). Cross-sectional and top-down SEM images of Ni foams obtained after 5, 10, 20, 40, and 60 s of deposition at $j_{geo} = -3$ A cm^{-2} are presented in Fig. 2, demonstrating the evolution of foam morphology as a function of the deposition time (additional data in Fig. S8). A deposition time of 5 s, corresponding to an average Ni film thickness of ~1 μm, was clearly insufficient to develop a full 3D foam structure. Only after 10 s did a network of interconnected open pores begin to evolve. In accordance with other examples of metal foam deposition processes

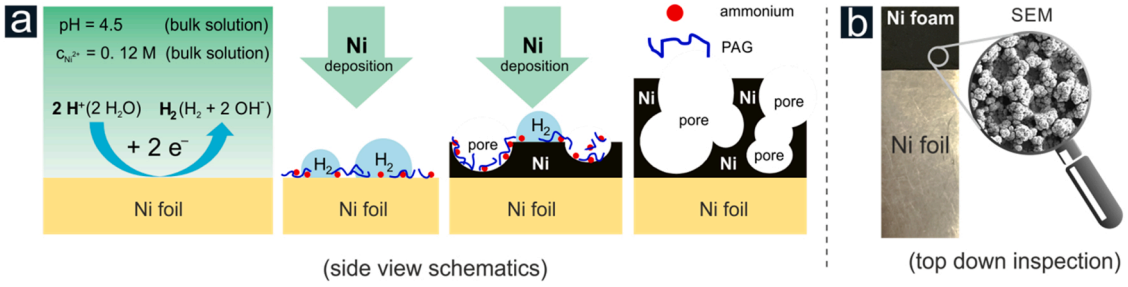

Fig. 1. a) Schematic drawing demonstrating the basic concept of the dynamic hydrogen bubble template (DHBT) and additive (*e.g.*, polyalkylene glycol, PAG) assisted metal foam deposition. b) Optical and SEM micrographs of a representative Ni foam deposited on a Ni foil support electrode.

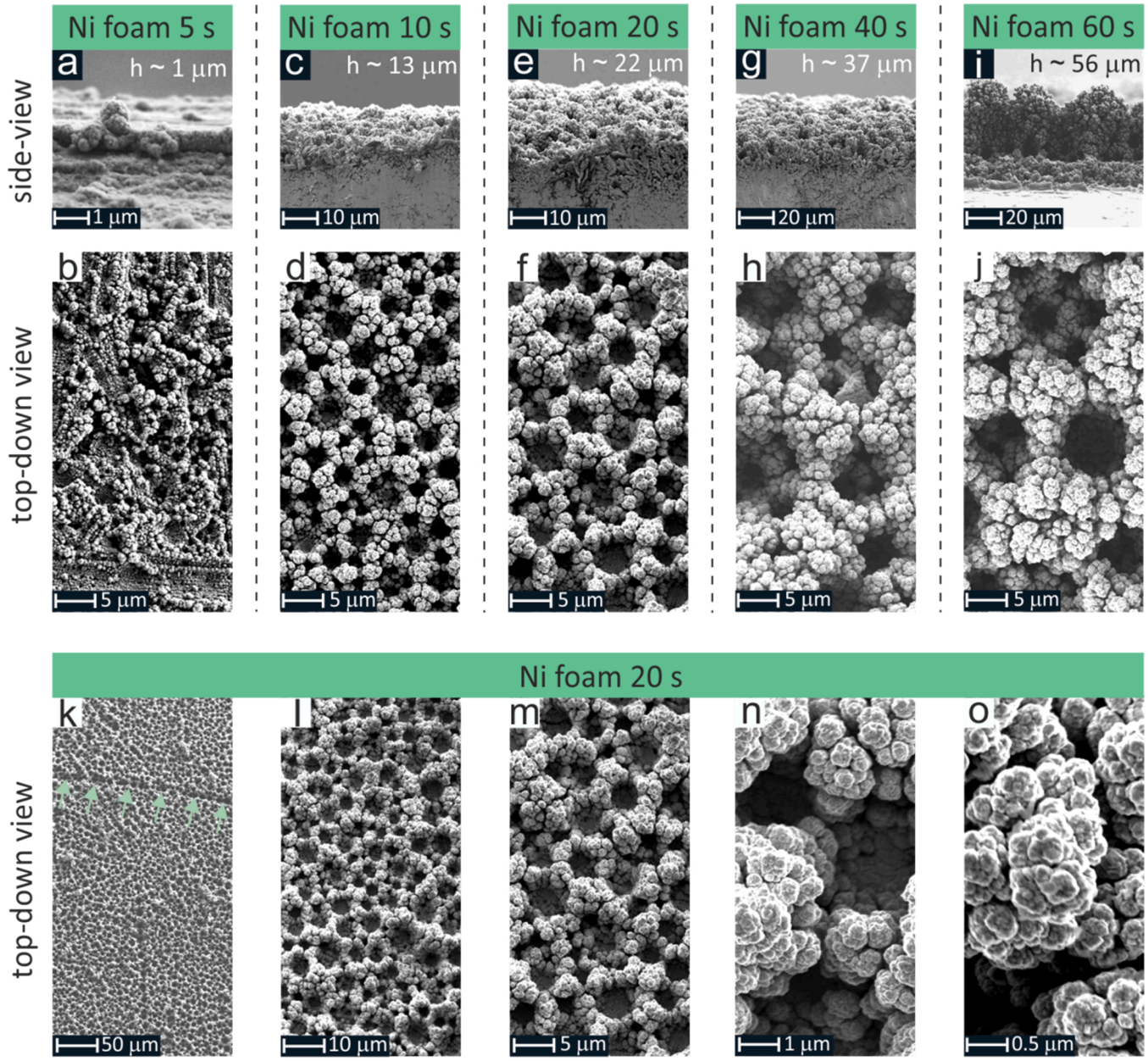

Fig. 2. a–j) Cross-sectional and top-down SEM micrographs showing the evolution of the foam morphology as a function of the deposition time (complete data set presented in Fig. S8). k–o) Top-down SEM micrographs of increasing magnification, showing the structural and morphological characteristics of the Ni foam yielded after 20 s of deposition. The green arrows in panel k indicate local imperfections in the foam structure originating from surface scratches in the Ni support (Fig. S1).

(Dutta et al., 2020b, 2016; Shin et al., 2004; Shin and Liu, 2004), the surface pore diameter of the Ni foam increased with deposition time, as a consequence of the continual coalescence of the templating hydrogen bubbles, in this particular case from ~2.6 μm (10 s) to ~8.2 μm (60 s). This increase in the mean surface pore diameter was accompanied by an increase in the foam film thickness and Ni mass loading from ~13 μm (10 s) to ~56 μm (60 s), and from 0.7 and 7.2 mg cm^{-2}, respectively (Fig. S9).

As demonstrated in Fig. 2k for the 20 s deposition case, the formed Ni foams typically showed high homogeneity across the Ni foil support. The Ni pore side-walls were composed of more "loosely" packed Ni clusters, thereby introducing a secondary porosity on the nanometer length scale, which was particularly pronounced in the case of the thicker Ni foams (40 s and 60 s of deposition). Aggregates of these Ni clusters have a cauliflower-like appearance (*e.g.*, Fig. 2o). According to complementary X-ray powder diffraction analyses (Fig. S10), the crystallinity of the obtained Ni foams was largely independent on the foam layer thickness (deposition time) and resembled the characteristics of polycrystalline Ni. Similar to other foam materials reported in the literature (Dutta et al., 2021a, 2016), a gradient in pore diameters formed along the surface normal. Structural data on the formed Ni foams are summarized in Fig. S8 and Fig. S9, and Table S1.

The highly porous nature of the electrodeposited Ni foams led to a substantial increase in the surface area. The electrochemically active surface area (ECSA), the fraction of the total surface area that is accessible to the aqueous electrolyte and consequently can participate in the electrolysis reaction, is particularly relevant to the electrolysis application. Therefore, the ECSA is a key parameter in the optimization of the catalyst material, because it scales with the number of active sites where the electrolysis reaction can occur. In this work, we applied two complementary voltammetric approaches for ECSA determination, on the basis of the measurement and analysis of either capacitive or Faradaic processes (details in the Experimental section). Results of the capacitance method approach (Fig. S5 and Table S1) indicated an increase in the ECSA from 5.44 cm^2 to 12.05 cm^2 when the deposition time was extended from 5 to 40 s. This trend in increasing surface area was confirmed through a complementary approach using the reversible reduction of dimethyl viologens as a "Faradaic" probe. Scan-rate dependent peak currents (I_p) were derived from the respective voltammograms (Fig. S6) and plotted against the square root of the applied potential sweep rate ($\nu^{1/2}$). The corresponding I_p *vs.* $\nu^{1/2}$ plots were linear in all cases, thus verifying that the Randles-Ševčík equation could be applied to these non-planar and highly porous electrode materials. The obtained ECSA values were in good agreement with those derived from the capacitive measurements, and changed from 6.78 cm^2 to 13.03 cm^2 with an increase in deposition time from 5 to 40 s (Table S1).

3.2. Catalytic performance of the Ni foams toward NO_3^- RR at pH 14

To evaluate the dependence of the electrocatalytic performance on foam morphology, we initially performed potentiostatic electrolyses at two selected potentials of –0.1 and –0.3 V *vs.* RHE. For this purpose, 1 M KOH (pH 14) solution containing 0.1 M KNO_3 as the nitrate source was used as the electrolyte. According to common protocols for NO_3^-RR catalyst screening (*e.g.*, Wang et al., 2020) strong alkaline conditions were established to suppress parasitic HER concurrent with the NO_3^-RR in this potential regime. Results obtained for these strongly alkaline experimental conditions enabled comparison with the performance of other benchmark NO_3^-RR catalysts reported in the literature (discussion below).

Fig. 3a depicts the resulting (mean) geometric electrolysis current densities (TCD_{geo}) as a function of the elapsed Ni deposition time (and therefore the Ni foam thickness). For both applied electrolysis potentials, an increase in TCD_{geo} with the deposition time was observed. This trend was associated with changes in the ECSA, which scaled with the time duration of the metal foaming process (Fig. S6, Table S1). However, when normalized to the ECSA, the TCD values became largely independent of the morphological properties (primary/secondary porosity, film thickness, *etc.*) of the Ni foams (Fig. S11). The plot of the corresponding FE_{NH3} values for ammonia production (Fig. 3b) indicated a

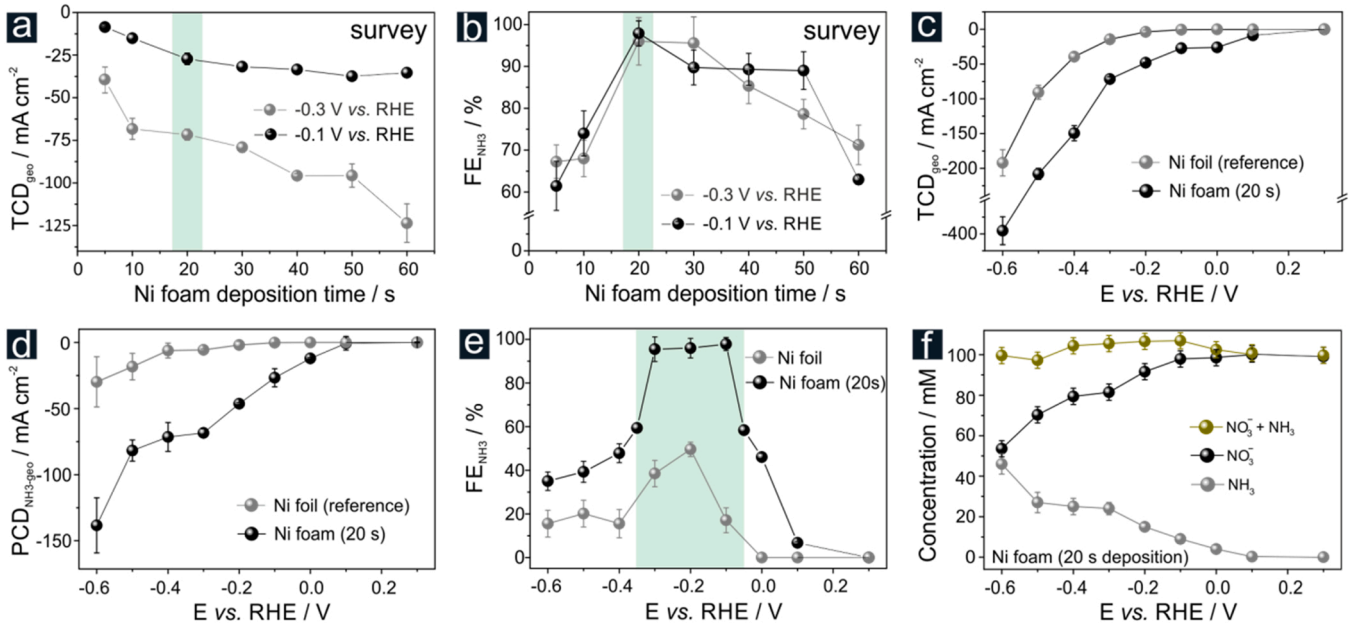

Fig. 3. a) Mean total electrolysis current densities (denoted TCD_{geo}, normalized to the geometric surface area of 1 cm^2), determined at electrolysis potentials of –0.1 and –0.3 V *vs.* the RHE. Resulting TCD_{geo} values are shown as a function of Ni foam deposition time. b) Faradaic efficiencies of ammonia production (FE_{NH3}), corresponding to panel a. c) Potential dependent (mean) total current densities (TCD_{geo}), determined for the blank Ni foil (reference) and the optimized Ni foam (20 s deposition time). c) Potential-dependent partial current densities of ammonia formation ($PCD_{NH3\text{-}geo}$) corresponding to panel c. d) Potential-dependent Faradaic efficiencies of ammonia formation (FE_{NH3}) corresponding to panel c and d. f) Nitrate and ammonia concentrations detected in the electrolyte after the potential dependent electrolysis. The time duration of the electrolysis experiments presented in Fig. 3 was 30 min (the numerical data associated to Fig. 3 can be found in Table S2–S5).

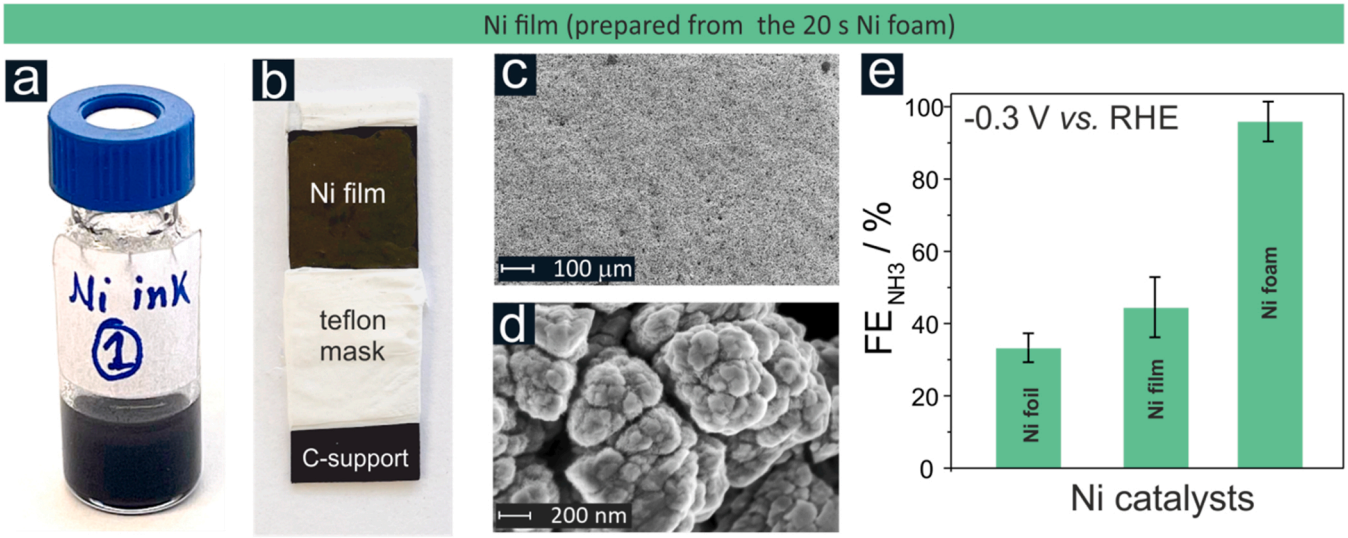

Fig. 4. a) Ni ink prepared from the Ni Foam (20 s deposition time). b) Ni film deposited on a carbon support. c)–d) Top-down SEM images of the Ni film catalyst; e) Comparison of the Faradaic efficiencies following 30 min electrolysis at −0.3 V *vs.* RHE.

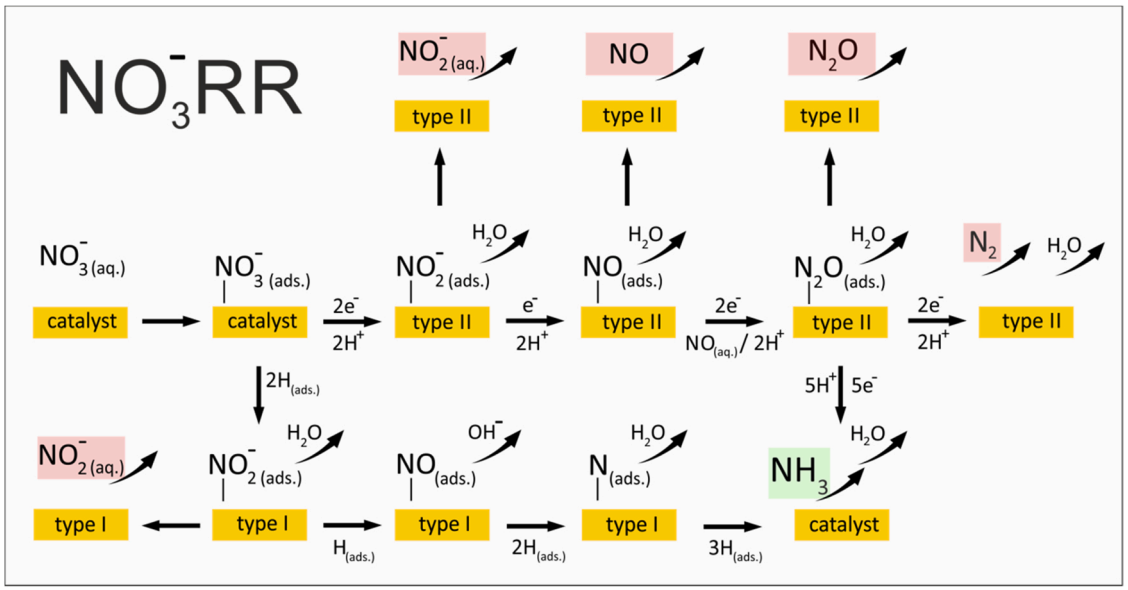

Fig. 5. Possible NO_3^-RR mechanisms. The targeted NO_3^-RR product (ammonia) is highlighted in green, and the non-desired by-products are highlighted in red. Type I catalysts include Pt, Pd, and Ru. Type II catalysts include Cu.

performance optimum in the range of 20–30 s of Ni foam deposition. For example, for the 20 s case, outstanding Faradaic ammonia yields of FE_{NH3} = 97.89% and FE_{NH3} = 95.99% were obtained for applied electrolysis potentials of −0.1 V and −0.3 V *vs.* RHE, respectively. To verify that the detected ammonia arose exclusively from the reduction of nitrate, we performed reference electrolysis by using a nitrate-free supporting electrolyte (Fig. S12 and S13). As expected, no ammonia could be detected when the electrolysis was carried out over the Ni foams in the nitrate-free electrolyte solution. These results are in full agreement with the recent work by Zheng et al. [Zhang et al. (2021)] who applied NMR techniques and ^{15}N labeled nitrate as the reactant to prove that the ammonia stems indeed from the electrochemical nitrate reduction over activated Ni catalysts.

A full potential dependent characterization of the catalyst performance (20 s deposition sample; Fig. 3c,d) demonstrated a sharp increase in the (total) electrolysis current density with increasing cathodic potential (Fig. 3c). To provide a reference, we collected corresponding data for the Ni foil support, which, in full agreement with the observed differences in the ECSA values (Fig. S6, Table S1), revealed substantially lower total electrolysis current densities. Similar potential-dependent trends were observed for the corresponding partial current densities of ammonia production ($PCD_{NH3\text{-}geo}$; Fig. 3d). $PCD_{NH3\text{-}geo}$ values were calculated from the corresponding FE_{NH3} values (Fig. 3e) and the corresponding total current densities (Fig. 3d). For both the Ni foil reference and the optimized Ni foam catalyst, a characteristic peak-like behavior was observed in the FE_{NH3} *vs.* E plot, with the ammonia selectivity maximum centered at approximately −0.2 V *vs.* RHE. In the case of the Ni foam, the Faradaic ammonia yields did not fall below 95%, even within a relatively broad potential range (~200 mV wide plateau region) spanning from −0.1 V to −0.3 V *vs.* RHE, with a maximum of 97.89% at −0.1 V *vs.* RHE. In comparison, the Faradaic yields determined for the Ni foil reference remained at substantially lower levels within the entire potential range studied, with a maximum of only 49.5% at −0.2 V *vs.* RHE. Notably, the novel Ni foam catalyst

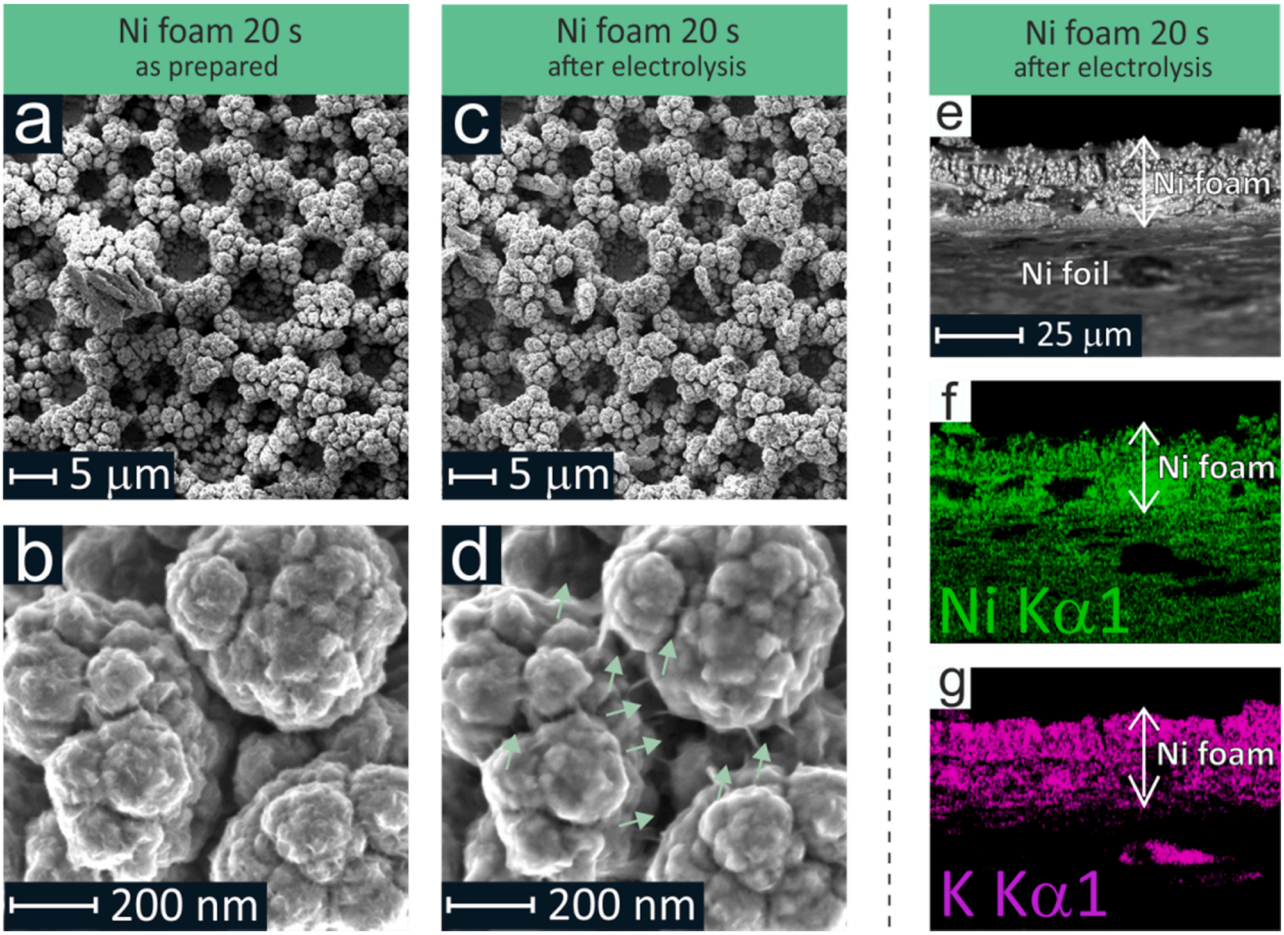

Fig. 6. a–d) Identical location (IL) top-down SEM characterization of the Ni foam catalyst (20 s deposition time) before and after electrolysis (30 min at −0.3 V *vs.* RHE). e–f) Cross-sectional SEM and 2D-EXD analysis of the Ni foam after the electrolysis. The K mapping (panel f) indicates wetting of the Ni foam catalyst down to the Ni foil support.

outperformed not only the planar foil but also the corresponding pure Ni catalysts reported in the literature (Wang et al., 2020). We assume that the steep decrease in FE_{NH3} values observed for the Ni foam and foil at potentials below −0.3 V *vs.* RHE (Fig. 3e) was due to the increasingly dominating HER, which at pH 14 was fed mainly by the reductive water splitting (reaction R5). This scenario was further corroborated by voltammetric reference measurements recorded for Ni foams (20 s) in the absence (blank) or presence of nitrate in the working electrolyte, which showed an onset of massive HER in 1 M KOH at potentials below −0.2 V *vs.* RHE (Fig. S13). In addition to these parasitic HER effects, nitrate mass transport limitations toward and into the Ni foam might become effective during NO_3^-RR at high cathodic potentials (high cathodic current densities), particularly when batch reactors with small electrolyte volume (7 mL) and a quiescent electrolyte (no convective mass transport) are used, thus further decreasing the respective ammonia Faradaic yields (Fig. 3e). Of note, in contrast to NO_3^-RR, the competing water splitting reaction does not become mass transport limited.

To exclude nitrogen containing NO_3^-RR products other than ammonia (*e.g.*, N_2, NO,N_2O, N_2H_4, or NO_2^-), we performed the ammonia analysis in tandem with the quantification of nitrate and nitrite concentrations by using post-electrolysis ion chromatography. The results (Fig. 3 f, Table S8) demonstrated that the detected ammonia (NO_3^-RR product) and nitrate (NO_3^-RR reactant) concentrations indeed reached approximately 100 mM, within the margins of error, over the entire potential range studied. Of note, an initial nitrate concentration of 100 mM was used for all electrolysis experiments presented in Fig. 3. These analyses demonstrated 100% selectivity for the (nitrate→ammonia) conversion with the use of the novel Ni foam catalyst. The NO_2^- concentration in all cases remained below the detection limit of the ion chromatographic analysis (Fig. S14). These results corroborated our conclusion that ammonia was the only nitrogen-containing product of the electrolysis reaction. Selected online gas-chromatography analysis confirmed that hydrogen was indeed the main parasitic by-product of the NO_3^-RR over Ni (Fig. S15). The massive formation of other gaseous nitrogen-containing products (*e.g.*, NO, N_2O, and dinitrogen) could therefore reasonably be excluded.

The presented electrolysis data (Fig. 3, Table S2 and Table S3) revealed that not only the catalyst's chemical nature and composition, but also its morphology on various length scales influences the resultant product selectivity. A similar dependence of the foam morphology on the product distribution has been reported for other pH dependent multi-step electrolysis reactions, *e.g.*, by Dutta et al. for the CO_2 reduction reaction (CO_2RR) performed over electrodeposited Cu foams with varying porosity (Dutta et al., 2016). In that case, improved hydrocarbon selectivity has been observed for the applied Cu foams (in comparison to respective planar catalysts)—an effect attributable to the trapping and readsorption of key CO_2RR intermediates (*e.g.*, CO, C_2H_4) inside the pores of the 3D foam catalyst (Dutta et al., 2016).

One possible scenario contributing to the observed excellent catalytic performance of the Ni foam is, in analogy to the CO_2RR/Cu foam case (Dutta et al., 2016), the trapping of formed and partially released NO_3^-RR intermediates (*e.g.*, NO_2^-, NO, N_2O) inside the 3D Ni foam catalyst. To experimentally corroborate this working hypothesis, we compared electrolysis experiments performed with the electrodeposited

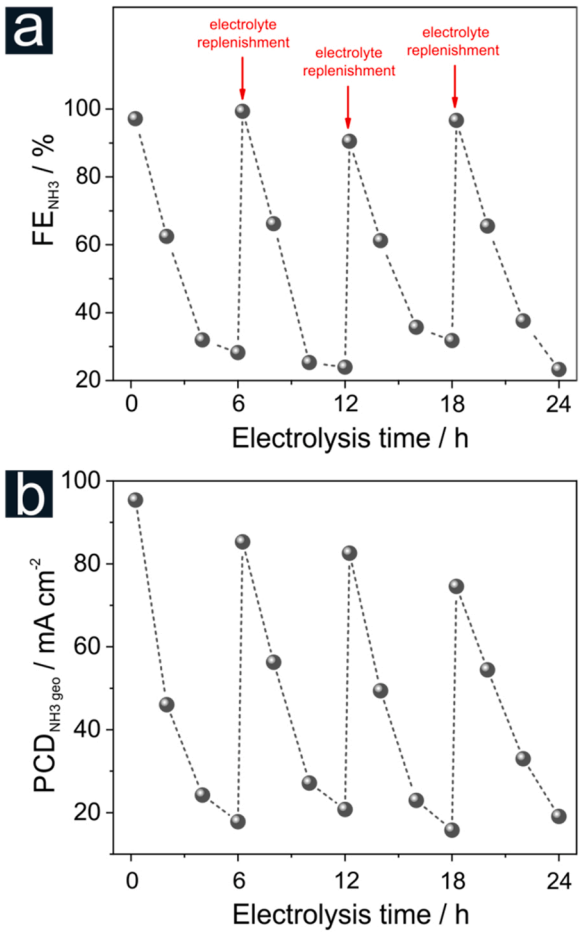

Fig. 7. Discontinuous long-term stress experiment of the 20 s Ni foam catalyst. The electrolyses were performed for 24 h in 1 M KOH + 0.1 M KNO_3 solution at an applied constant potential of −0.3 V *vs.* RHE. As indicated in the graph, the electrolyses were interrupted at certain electrolysis times, and the electrolyte was replenished in intervals of 6 h. This procedure also involved the replenishment of the electrolyte inside the Ni foam. a) Time-dependent Faradaic efficiency of ammonia production. b) Corresponding partial current densities of ammonia production.

Ni foam (20 s deposition time) to Ni film catalysts in which the primary macroporosity was intentionally eliminated, whereas the morphological characteristics on the nanometer length scale remained conserved (Fig. 4 and Fig. S16). Clearly, the porous foam type of Ni catalysts outperformed the Ni film catalyst fabricated from the respective foam materials, thus confirming that the primary macroporosity plays an eminent role in the overall NO_3^-RR performance.

Interestingly, the maximum Faradaic ammonia yield (FE_{NH3}) was reached at slightly lower applied electrolysis potentials when the Ni foam was used as the catalyst, thus indicating more energy efficient (nitrate→ammonia) conversion on the Ni than with, *e.g.*, the Cu based catalysts (*e.g.*, Cu/Cu_2O-NWs, FE_{NH3} = 95.8%, E = –0.85 V *vs.* RHE;) (Wang et al., 2020). Further information for reference is provided in Fig. S17 and Table S6.

Fig. 5 displays possible reaction pathways discussed in the literature for a variety of NO_3^-RR catalysts. In general, two groups of NO_3^-RR catalysts can be distinguished. The first class, including metals that are highly active toward the HER (*e.g.*, Pd, Pt, and Ru, denoted type I in Fig. 5), reduce nitrate through a hydrogenation reaction pathway involving (pre)adsorbed (atomic) hydrogen (Zhang et al., 2021). This aspect might also explain why the NO_3^-RR yields reported for these catalysts are substantially lower than those for, *e.g.*, Cu. The direct competition of adsorbed H and NO_3^- for surface adsorption sites prevents higher Faradaic yields for these metals. Recombination of adsorbed H species (instead of NO_x hydrogenation) promotes parasitic HER. On metals such as Cu (denoted type II in Fig. 5), the metal-H bonding is much weaker than that on the first group of metallic catalysts. Therefore, higher surface concentrations of adsorbed NO_3^- might be achieved in the case of Cu, which in turn could further suppress the parasitic HER through sterically blocking the respective active sites. In the case of Cu, protons are transferred from the solution phase to the adsorbed (and partially reduced) NO_x species. Of note, both hydronium cations and water could, in principle, serve as the proton source for the coupled electron/proton transfer reaction (depending on the solution pH). Although Ni is known to be highly active toward HER, we observed that the novel Ni foams showed extraordinarily strong HER suppression (Fig. 3e). Generally, these findings are in excellent agreement with recent experimental observations made by Zheng et al. reporting on the effective suppression of the HER over self-activated Ni cathodes [Zhang et al., 2021]. Based on kinetic considerations in combination with DFT calculations Zheng et al. postulated an NO_3^-RR mechanism for the self-activated Ni catalysts resembling characteristics of the type I pathway (Fig. 5) typical for the more precious metal catalysts. A key aspect of their proposed mechanism is the *in situ* and surface-confined formation of nanoparticulate $Ni(OH)_2$ as the catalytically active component on the metallic Ni support. Assuming a $Ni(OH)_2(101)$ model system, DFT calculations indeed suggested a lower kinetic barrier height for the atomic H mediated reduction mechanism (type I in Fig. 5) compared to the competing electron transfer pathway (type II) [Zhang et al., 2021]. Although we do not have direct experimental evidence for the involvement hydroxide or oxidic Ni species in the NO_3^-RR (*e.g.*, see Fig. S18) we cannot exclude their *in situ* formation during NO_3^-RR also on the novel Ni foams addressed herein (see also discussion below). A complementary *operando* analytical approach is required to ultimately clarify this mechanistic aspect and to reveal in particular the potential-dependent stability of possibly formed $Ni(OH)_2$ against electroreduction under these cathodic conditions (as a prime example of this approach see Dutta et al. (2020b)).

The model proposed by Zheng et al. convincingly rationalizes the strong HER suppression over activated Ni. It does, however, not reflect in the present case the eminent mechanistic role of the foam macroporosity on the NO_3^-RR performance (Fig. 4) and the related further boost of the ammonia Faradaic efficiency reported herein (Fig. 3).

3.3. Stability of the Ni foam catalysts during extended NO_3^-RR

To test the structural stability of the Ni foam catalysts, we performed an extended 6 h electrolysis at −0.3 V *vs.* RHE (Fig. S19). The identical location (SEM) technique (Rahaman et al., 2017) was applied to examine the morphology of the Ni foam at the same location on the catalyst surface before and after 6 h of electrolysis (Fig. 6a–d). In general, the novel Ni foam catalysts demonstrated high structural stability during NO_3^-RR. The primary macroporosity remained completely unaffected by the extended electrolysis. Only marginal changes in morphology on the nanometer length scale were observed, which may arose from trace electrolyte residues (drying effect) or from the formation of a surface hydroxide layer (discussion above).

This study is the first report on the use of cross-sectional SEM/2D-EDX analysis to study the wetting behavior of a foam catalyst (Fig. 6e–g). For this purpose, we applied two-dimensional EDX mapping of potassium to probe the electrolyte penetration (1 M KOH + 0.1 M KNO_3) into the 3D structure of the Ni foam. The 2D potassium mapping (Fig. 6g) indicated that the full 3D structure of the Ni foam was wetted by the electrolyte down to the Ni foil support. The same behavior was observed for even the thickest Ni foam applied in this study (60 s deposition time, Fig. S20). Of note, the FE_{NH3} decreased over the course of electrolysis. This finding can be explained by (i) the consumption of the nitrate reactant in the working electrolyte and, more importantly,

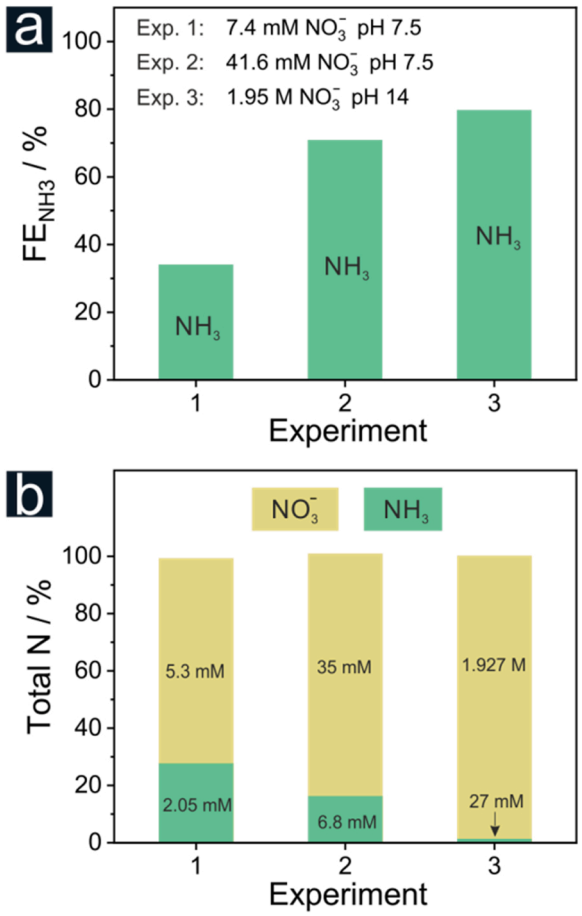

Fig. 8. Catalyst screening experiments (30 min duration at −0.3 V *vs.* RHE) were carried out using the optimized Ni foam catalyst (20 s deposition time). The electrolyte composition was varied to mimic wastewater conditions (Exp. 1: $c_{nitrate}$ = 7.4 mM, pH 7.5; Exp. 2: $c_{nitrate}$ = 41.6 mM, pH 7.5; Exp. 3: $c_{nitrate}$ = 1.95 M, pH 14). b) Total nitrogen content (%) derived from the analysis of the ammonia and nitrate contents demonstrating a close to 100% (nitrate→ammonia) selectivity. The obtained nitrate and ammonia concentrations are indicated in the graph.

(ii) the depletion of nitrate inside the 3D foam catalyst during extended NO_3^-RR. Therefore, the product selectivity shifted from predominant ammonia production (initial stage) toward hydrogen evolution (final stage) during extended continuous electrolysis.

However, high Faradaic yields of ammonia production can in principle be recovered by electrolyte replenishment, as demonstrated in Fig. 7, in a more extended (discontinuous) catalyst stressing experiment. Two forms of catalyst stress were applied in this experiment: one through the extended electrolysis itself (24 h duration in total), and a second more extreme form of stress from the repetitive switching off the electrolysis reaction, also involving the loss of potential control at given electrolysis times (*e.g.*, for the electrolyte replenishment). However, the electrolysis data (Fig. 7) suggested that the Ni foam was sufficiently robust to withstand these various forms of stress. The initial ammonia efficiency of FE_{NH3} = 95.4% (25 min) decreased within 6 h of electrolysis to FE_{NH3} = 17.8% but fully recovered after the first electrolyte replenishment (FE_{NH3} = 99% at 6 h 25 min). After the third electrolyte replenishment, the ammonia yield was initially still above 90%. In general, the corresponding partial current densities of ammonia production (Fig. 7b) followed the overall trend of Faradaic efficiencies, thus supporting our working hypothesis that reactant depletion in the electrolyte and the foam interior caused the performance losses observed during continued electrolysis. Of note, we observed a slight decrease in $PCD_{NH3\text{-}geo}$ values from an initial 95.3 mA cm^{-1} (after 25 min) to 74.6 mA cm^{-1} (after 18 h 25 min; after the third replenishment).

Post-electrolysis analyses of the used catholytes revealed only negligible Ni corrosion during the extended NO_3^-RR. The Ni content in the electrolytes in each case remained below the detection limit of the ICP-MS analysis (~0.5 ppb). The stability of the catalysts against corrosion, *e.g.*, in the form of losses of metallic catalysts into the aqueous electrolyte, is of paramount importance for any future application (*e.g.*, wastewater treatment) [Zhang et al. (2021)].

3.4. Catalytic performance of the Ni foams toward NO_3^-RR under relevant wastewater conditions

The catalyst screening experiments described above were performed under strongly alkaline electrolyte conditions (pH 14) and relatively high nitrate conditions, with the aim to reveal the intrinsic catalytic characteristics of the Ni foam, particularly regarding the effects of foam morphology on the overall performance (Fig. 3). This initial catalyst screening approach further enabled us to identify the optimum potential range for nitrate electrolysis under ideal experimental conditions. However, van Langevelde et al. have indicated that much lower nitrate concentrations at near neural pH must be used to test catalyst performance under more realistic wastewater conditions (van Langevelde et al., 2021). For example, the NO_3^- concentrations in textile and industrial wastewater are typically 7.4 and 41.6 mM, respectively, whereas their solution pH varies from 7 to 7.9. Therefore, we performed additional electrolyses at −0.3 V *vs.* RHE and pH 7.5 with the optimized Ni foam catalyst (20 s deposition time). The nitrate concentrations were 7.4 and 41.6 mM, respectively, to mimic textile and industrial wastewater conditions (Fig. 8, experiments 1 and 2). The resulting Faradaic ammonia yields of 34% ($c_{nitrate}$ = 7.4 mM) and 71% ($c_{nitrate}$ = 41.6 mM), as expected, were lower than those observed in the ideal electrolysis conditions (FE_{NH3} = 95.99% at $c_{nitrate}$ = 100 mM and pH 14; Fig. 3). The reason for this lower performance was the lower nitrate concentration and lower pH, both of which favored the competing HER, which occurred in parallel to the NO_3^-RR at this electrolysis potential. The Faradaic yields obtained with the novel Ni foams (Fig. 8, experiments 1 and 2) were comparable or even superior to the catalyst performance reported in the literature for other catalyst materials. For example, Su et al. have reported a maximum FE_{NH3} of 36% for a Ti supported Co_3O_4 catalyst by using a 7.4 mM nitrate electrolyte (Su et al., 2017). Chauhan et al. have achieved a comparably low Faradaic ammonia yield of only 6% by using iron as the catalyst and a 41.6 mM nitrate containing electrolyte solution (Chauhan et al., 2020). This comparison clearly demonstrates that the excellent catalytic performance of the novel Ni foams observed under ideal experimental conditions (Fig. 3) was also preserved in screening experiments mimicking real wastewater conditions (Fig. 8). This finding was notably true for the near to unity (nitrate→ammonia) selectivity with no other nitrogen containing products (*e.g.*, NO_2^-) detected. Again, this conclusion was derived from the ammonia quantification in combination with nitrate (reactant) concentration monitoring.

Finally, we extended our catalyst screening experiments to experimental conditions mimicking nuclear wastewater conditions ($c_{nitrate}$ = 1.95 M, pH 14, experiment 3 in Fig. 8). (van Langevelde et al., 2021) Excellent ammonia yields were achieved (FE_{NH3} = 80%) also under these experimental conditions.

4. Conclusions

In this work, we report the first application of an additive and DHBT assisted electrodeposition process to produce Ni foam catalysts for highly efficient and selective (nitrate→ammonia) electroreduction (NO_3^-RR). Optimized Ni foams (20 s deposition time) under ideal electrolyte conditions ($c_{nitrate}$ = 100 mM, pH 14) revealed an outstanding

FE_{NH3} remaining above 95% within a relatively broad potential window of ~200 mV ranging from –0.1 to −0.3 V *vs.* RHE. The highest efficiencies, *e.g.*, FE_{NH3} = 95.99% at −0.3 V *vs.* RHE, were observed at applied electrolysis potentials slightly more positive than those reported for pure Cu catalysts, which are often considered the benchmark for NO_3^-RR. The porous nature of the Ni foams was associated with a high ECSA and thus was determined to be the physical origin of the observed superior (initial) partial current densities of ammonia production (*e.g.*, PCD_{NH3} = −68.4 mA cm^{-2} at −0.3 V *vs.* RHE; PCD_{NH3} = −138.3 mA cm^{-2} at −0.6 V *vs.* RHE).

Post-electrolysis cross-sectional EDX mapping (K tracing) provided the first experimental demonstration of the complete wetting of this type of foam catalyst by the working electrolyte, down to the layer of the planar support material.

Extended 24-hour nitrate electrolysis indicated the excellent stability of the Ni foam catalyst. These results were consistent with those from microscopic analyses performed at the same location of the catalyst before and after electrolysis (through the IL approach).

Our forthcoming studies will apply *operando* spectroscopic means (specifically X-ray absorption spectroscopy, infrared and Raman vibrational spectroscopy) to reveal the mechanistic origin of the high Faradic ammonia yields, as observed on the Ni foam. To address the observed nitrate mass transport effects toward and into the 3D Ni foam, and the associated losses in the Faradaic yields of ammonia production during extended electrolyses, we will replace the batch reactor design used for the initial catalyst screening herein with more sophisticated electrolyte flow-cell devices, with the aim to maintain the observed high partial current densities and high Faradaic efficiencies of ammonia production during extended electrolyses.

Declaration of Competing Interest

The authors declare that they have no known competing financial interests or personal relationships that could have appeared to influence the work reported in this paper.

Data Availability

The raw data associated this work can be found online at DOI. 10.5281/zenodo.6659731.

Acknowledgments

This publication was created as part of NCCR Catalysis (grant number 180544), a National Centre Competence in Research funded by the Swiss National Science Foundation. A.I. acknowledges financial support from the State Secretariat for Education, Research and Innovation through a Swiss Government Excellence Scholarship for Foreign Scholars.

Supplementary material

Additional figures (Figs. S1–S20) and tables (Table S1–S6) can be found online.

Appendix A. Supporting information

Supplementary data associated with this article can be found in the online version at doi:10.1016/j.jhazmat.2022.129504.

References

Abdallah, R., Geneste, F., Labasque, T., Djelal, H., Fourcade, F., Amrane, A., Taha, S., Floner, D., 2014. Selective and quantitative nitrate electroreduction to ammonium using a porous copper electrode in an electrochemical flow cell. J. Electroanal. Chem. 727, 148–153. https://doi.org/10.1016/j.jelechem.2014.06.016.

Bunea, S., Clemens, K., Urakawa, A., 2022. Electrified conversion of contaminated water to value: selective conversion of aqueous nitrate to ammonia in a polymer electrolyte membrane cell. ChemSusChem 15 (2), e202102180. https://doi.org/10.1002/cssc.202102180.

Canfield, D.E., Glazer, A.N., Falkowski, P.G., 2010. The evolution and future of earth nitrogen cycle. Science 330 (6001), 192–196. https://doi.org/10.1126/science.1186120.

Chauhan, R., Srivastava, V.C., 2020. Electrochemical denitrification of highly contaminated actual nitrate wastewater by Ti/RuO2 anode and iron cathode. Chem. Eng. J. 386, 122065 https://doi.org/10.1016/j.cej.2019.122065.

Dima, G.E., de Vooys, A.C.A., Koper, M.T.M., 2003. Electrocatalytic reduction of nitrate at low concentration on coinage and transition-metal electrodes in acid solutions. J. Electroanal. Chem. 554–555, 15–23. https://doi.org/10.1016/S0022-0728(02)01443-2.

Dong Xu, Y.L., Yin, Lifeng, Ji, Yangyuan, Niu, Junfeng, Yu, Yanxin, 2018. Electrochemical removal of nitrate in industrial wastewater. Front. Environ. Sci. Eng. 12 (1), 9-. https://doi.org/10.1007/s11783-018-1033-z.

Duca, M., Koper, M.T.M., 2012. Powering denitrification: the perspectives of electrocatalytic nitrate reduction. Energy Environ. Sci. 5 (12), 9726–9742. https://doi.org/10.1039/C2EE23062C.

Dutta, A., Kiran, K., Rahaman, M., Montiel, I.Z., Moreno-García, P., Vesztergom, S., Drnec, J., Oezaslan, M., Broekmann, P., 2021a. Insights from operando and identical location (IL) techniques on the activation of electrocatalysts for the conversion of CO_2: a mini-review. Chimia Int. J. Chem. 75 (9), 733–743. https://doi.org/10.2533/chimia.2021.733.

Dutta, A., Montiel, I.Z., Erni, R., Kiran, K., Rahaman, M., Drnec, J., Broekmann, P., 2020a. Activation of bimetallic AgCu foam electrocatalysts for ethanol formation from CO_2 by selective Cu oxidation/reduction. Nano Energy 68, 104331. https://doi.org/10.1016/j.nanoen.2019.104331.

Dutta, A., Rahaman, M., Hecker, B., Drnec, J., Kiran, K., Zelocualtecatl Montiel, I., Jochen Weber, D., Zanetti, A., Cedeño López, A., Martens, I., Broekmann, P., Oezaslan, M., 2020b. CO_2 electrolysis – complementary operando XRD, XAS and Raman spectroscopy study on the stability of CuxO foam catalysts. J. Catal. 389, 592–603. https://doi.org/10.1016/j.jcat.2020.06.024.

Dutta, A., Rahaman, M., Luedi, N.C., Mohos, M., Broekmann, P., 2016. Morphology matters: tuning the product distribution of CO_2 electroreduction on oxide-derived Cu foam catalysts. ACS Catal. 6 (6), 3804–3814. https://doi.org/10.1021/acscatal.6b00770.

Dutta, A., Rahaman, M., Mohos, M., Zanetti, A., Broekmann, P., 2017. Electrochemical CO_2 conversion using skeleton (Sponge) type of Cu catalysts. ACS Catal. 7 (8), 5431–5437. https://doi.org/10.1021/acscatal.7b01548.

Dutta, A., Zelocualtecatl Montiel, I., Kiran, K., Rieder, A., Grozovski, V., Gut, L., Broekmann, P., 2021b. A tandem ($Bi_2O_3 \rightarrow B_{met}$) catalyst for highly efficient ec-CO_2 conversion into formate: operando Raman spectroscopic evidence for a reaction pathway change. ACS Catal. 11 (9), 4988–5003. https://doi.org/10.1021/acscatal.0c05317.

Epsztein, R., Nir, O., Lahav, O., Green, M., 2015. Selective nitrate removal from groundwater using a hybrid nanofiltration–reverse osmosis filtration scheme. Chem. Eng. J. 279, 372–378. https://doi.org/10.1016/j.cej.2015.05.010.

Galloway, J.N., Aber, J.D., Erisman, J.W., Seitzinger, S.P., Howarth, R.W., Cowling, E.B., Cosby, B.J., 2003. The nitrogen cascade. BioScience 53 (4), 341–356. https://doi.org/10.1641/0006-3568(2003)053[0341:tnc]2.0.co;2.

Galloway, J.N., Townsend, A.R., Erisman, J.W., Bekunda, M., Cai, Z., Freney, J.R., Martinelli, L.A., Seitzinger, S.P., Sutton, M.A., 2008. Transformation of the nitrogen cycle: recent trends, questions, and potential solutions. Science 320 (5878), 889–892. https://doi.org/10.1126/science.1136674.

Ghavam, S., Vahdati, M., Wilson, I.A.G., Styring, P., 2021. Sustainable ammonia production processes. Front. Energy Res 9. https://doi.org/10.3389/fenrg.2021.580808.

Gruber, N., Galloway, J.N., 2008. An Earth-system perspective of the global nitrogen cycle. Nature 451 (7176), 293–296. https://doi.org/10.1038/nature06592.

Jacks, G., Sharma, V.P., 1983. Nitrogen circulation and nitrate in groundwater in an agricultural catchment in Southern India. Environ. Geol. 5 (2), 61–64. https://doi.org/10.1007/BF02381097.

Jhong, H.-R.M., Ma, S., Kenis, P.J.A., 2013. Electrochemical conversion of CO_2 to useful chemicals: current status, remaining challenges, and future opportunities. Curr. Opin. Chem. Eng. 2 (2), 191–199. https://doi.org/10.1016/j.coche.2013.03.005.

Jones, E.R., van Vliet, M.T.H., Qadir, M., Bierkens, M.F.P., 2021. Country-level and gridded estimates of wastewater production, collection, treatment and reuse. Earth Syst. Sci. Data 13 (2), 237–254. https://doi.org/10.5194/essd-13-237-2021.

Kato, M., Okui, M., Taguchi, S., Yagi, I., 2017. Electrocatalytic nitrate reduction on well-defined surfaces of tin-modified platinum, palladium and platinum-palladium single crystalline electrodes in acidic and neutral media. J. Electroanal. Chem. 800, 46–53. https://doi.org/10.1016/j.jelechem.2017.01.020.

Katsounaros, I., Dortsiou, M., Kyriacou, G., 2009. Electrochemical reduction of nitrate and nitrite in simulated liquid nuclear wastes. J. Hazard. Mater. 171 (1), 323–327. https://doi.org/10.1016/j.jhazmat.2009.06.005.

Li, J., Zhan, G., Yang, J., Quan, F., Mao, C., Liu, Y., Wang, B., Lei, F., Li, L., Chan, A.W.M., Xu, L., Shi, Y., Du, Y., Hao, W., Wong, P.K., Wang, J., Dou, S.-X., Zhang, L., Yu, J.C., 2020. Efficient ammonia electrosynthesis from nitrate on strained ruthenium nanoclusters. J. Am. Chem. Soc. 142 (15), 7036–7046. https://doi.org/10.1021/jacs.0c00418.

Lu, X., Song, H., Cai, J., Lu, S., 2021. Recent development of electrochemical nitrate reduction to ammonia: a mini review. Electrochem. Commun. 129, 107094–107101. https://doi.org/10.1016/j.elecom.2021.107094.

Martín, A.J., Shinagawa, T., Pérez-Ramírez, J., 2019. Electrocatalytic reduction of nitrogen: from Haber-Bosch to ammonia artificial leaf. Chem 5 (2), 263–283. https://doi.org/10.1016/j.chempr.2018.10.010.

Qiao, J.L., Liu, Y.Y., Hong, F., Zhang, J.J., 2014. A review of catalysts for the electroreduction of carbon dioxide to produce low-carbon fuels. Chem. Soc. Rev. 43 (2), 631–675. https://doi.org/10.1039/c3cs60323g.

Rahaman, M., Dutta, A., Zanetti, A., Broekmann, P., 2017. Electrochemical Reduction of CO_2 into Multicarbon Alcohols on Activated Cu Mesh Catalysts: An Identical Location (IL) Study. ACS Catal. 7 (11), 7946–7956. https://doi.org/10.1021/acscatal.7b02234.

Reyter, D., Chamoulaud, G., Bélanger, D., Roué, L., 2006. Electrocatalytic reduction of nitrate on copper electrodes prepared by high-energy ball milling. J. Electroanal. Chem. 596, 13–24. https://doi.org/10.1016/j.jelechem.2006.06.012.

Samatya, S., Kabay, N., Yüksel, Ü., Arda, M., Yüksel, M., 2006. Removal of nitrate from aqueous solution by nitrate selective ion exchange resins. React. Funct. Polym. 66 (11), 1206–1214. https://doi.org/10.1016/j.reactfunctpolym.2006.03.009.

Shin, H.C., Dong, J., Liu, M., 2004. Porous tin oxides prepared using an anodic oxidation process. Adv. Mater. 16 (3), 237–240. https://doi.org/10.1002/adma.200305660.

Shin, H.C., Liu, M., 2004. Copper foam structures with highly porous nanostructured walls. Chem. Mater. 16 (25), 5460–5464. https://doi.org/10.1021/cm048887b.

Su, J.F., Ruzybayev, I., Shah, I., Huang, C.P., 2016. The electrochemical reduction of nitrate over micro-architectured metal electrodes with stainless steel scaffold. Appl. Catal. B 180, 199–209. https://doi.org/10.1016/j.apcatb.2015.06.028.

Su, L., Li, K., Zhang, H., Fan, M., Ying, D., Sun, T., Wang, Y., Jia, J., 2017. Electrochemical nitrate reduction by using a novel Co3O4/Ti cathode. Water Res 120, 1–11. https://doi.org/10.1016/j.watres.2017.04.069.

Taguchi, S., Feliu, J.M., 2007. Electrochemical reduction of nitrate on Pt(S)[n(111)×(111)] electrodes in perchloric acid solution. Electrochim. Acta 52 (19), 6023–6033. https://doi.org/10.1016/j.electacta.2007.03.057.

van Langevelde, P.H., Katsounaros, I., Koper, M.T.M., 2021. Electrocatalytic nitrate reduction for sustainable ammonia production. Joule 5 (2), 290–294. https://doi.org/10.1016/j.joule.2020.12.025.

Vesztergom, S., Dutta, A., Rahaman, M., Kiran, K., Zelocualtecatl Montiel, I., Broekmann, P., 2021. Hydrogen bubble templated metal foams as efficient catalysts of CO_2 electroreduction. ChemCatChem 13 (4), 1039–1058. https://doi.org/10.1002/cctc.202001145.

Wang, L., Xia, M., Wang, H., Huang, K., Qian, C., Maravelias, C.T., Ozin, G.A., 2018. Greening ammonia toward the solar ammonia refinery. Joule 2 (6), 1055–1074. https://doi.org/10.1016/j.joule.2018.04.017.

Wang, S., Ichihara, F., Pang, H., Chen, H., Ye, J., 2018. Nitrogen fixation reaction derived from nanostructured catalytic materials. Adv. Funct. Mater. 28 (50), 1803309. https://doi.org/10.1002/adfm.201803309.

Wang, Y., Xu, A., Wang, Z., Huang, L., Li, J., Li, F., Wicks, J., Luo, M., Nam, D.-H., Tan, C.-S., Ding, Y., Wu, J., Lum, Y., Dinh, C.-T., Sinton, D., Zheng, G., Sargent, E.H., 2020. Enhanced nitrate-to-ammonia activity on copper–nickel alloys via tuning of intermediate adsorption. J. Am. Chem. Soc. 142 (12), 5702–5708. https://doi.org/10.1021/jacs.9b13347.

Wang, Y., Zhou, W., Jia, R., Yu, Y., Zhang, B., 2020. Unveiling the activity origin of a copper-based electrocatalyst for selective nitrate reduction to ammonia. Angew. Chem. Int. Ed. 59 (13), 5350–5354. https://doi.org/10.1002/anie.201915992.

Whipple, D.T., Kenis, P.J.A., 2010. Prospects of CO_2 utilization via direct heterogeneous electrochemical reduction. J. Phys. Chem. Lett. 1 (24), 3451–3458. https://doi.org/10.1021/jz1012627.

Yang, J., Sebastian, P., Duca, M., Hoogenboom, T., Koper, M.T.M., 2014. pH dependence of the electroreduction of nitrate on Rh and Pt polycrystalline electrodes. Chem. Commun. 50 (17), 2148–2151. https://doi.org/10.1039/C3CC49224A.

Yang, S., Gruber, N., 2016. The anthropogenic perturbation of the marine nitrogen cycle by atmospheric deposition: Nitrogen cycle feedbacks and the 15N Haber-Bosch effect. Glob. Biogeochem. Cycles 30 (10), 1418–1440. https://doi.org/10.1002/2016GB005421.

Zhang, X., Wang, Y., Liu, C., Yu, Y., Lu, S., Zhang, B., 2021. Recent advances in non-noble metal electrocatalysts for nitrate reduction. Chem. Eng. J. 403, 126269 https://doi.org/10.1016/j.cej.2020.126269.

Zhang, Y., Zhao, Y., Chen, Z., Wang, L., Wu, P., Wang, F., 2018. Electrochemical reduction of nitrate via Cu/Ni composite cathode paired with Ir-Ru/Ti anode: High efficiency and N2 selectivity. Electrochim. Acta 291, 151–160. https://doi.org/10.1016/j.electacta.2018.08.154.

Zheng, W., Zhu, L., Yan, Z., Lin, Z., Lei, Z., Zhang, Y., Xu, H., Dang, Z., Wei, C., Feng, C., 2021. Self-activated Ni cathode for electrocatalytic nitrate reduction to ammonia: from fundamentals to scale-up for treatment of industrial wastewater. Environ. Sci. Technol. 55 (19), 13231–13243. https://doi.org/10.1021/acs.est.1c02278.

Zhu, W., Zhang, R., Qu, F., Asiri, A.M., Sun, X., 2017. Design and application of foams for electrocatalysis. ChemCatChem 9 (10), 1721–1743. https://doi.org/10.1002/cctc.201601607.